Journal of Positive Sciences (JPS) eISSN: 2582-9351, https://positive-sciences.com JPS. 2026 July; 6(4): 190-210

Article info
Received on: 17.06.2026
Accepted on: 09.07.2026
Published on: 12.07.2026
doi: https://doi.org/10.52688/JPS217894

Research Article

Design of Fe-Doped MgO Nanoparticles for Improved Antibacterial Applications

Rasha Noori Hammad [1], Mohammed RASHEED [2,*], Habiba Kadhim Aity [3]

[1] Microbiology, Education Baghdad Al-Karkh 2, Ministry of Education, Baghdad, Iraq
[2] College of Production Engineering & Metallurgy, University of Technology- Iraq, Baghdad, Iraq
[3] Scientific Research Commission, Baghdad, Iraq

[*] rasheed.mohammed40@yahoo.com

ABSTRACT

The rapid emergence of multidrug-resistant bacteria has intensified the search for alternative antimicrobial materials capable of overcoming conventional antibiotic limitations. Among various inorganic nanomaterials, magnesium oxide (MgO) nanoparticles have attracted considerable attention owing to their chemical stability, biocompatibility, low toxicity, and remarkable antibacterial activity. In this study, Fe-doped magnesium oxide nanoparticles with the composition $Mg_{0.94}Fe_{0.06}O$ were synthesized using a simple chemical preparation route followed by calcination at 550 °C. The influence of iron incorporation on the structural, optical, and antibacterial properties of MgO nanoparticles was systematically investigated. Fourier-transform infrared spectroscopy confirmed the formation of Mg–O bonds together with hydroxyl functional groups that facilitate surface interactions with bacterial membranes. UV–Visible spectroscopy revealed strong absorption in the ultraviolet region, while Tauc analysis estimated a direct optical band gap of approximately 3.96 eV, indicating the semiconductor nature of the prepared nanoparticles. Antibacterial activity was evaluated against the Gram-positive bacterium *Staphylococcus aureus* using the agar diffusion method. The synthesized nanoparticles exhibited a clear inhibition zone of approximately 15 mm, demonstrating effective antibacterial performance. The enhanced antibacterial activity is attributed to the synergistic effects of Fe doping, which promotes oxygen vacancy formation, increases reactive oxygen species generation, improves surface defect density, and strengthens interactions with bacterial cell walls. The relationship between structural characteristics and biological performance indicates that structural modifications induced by iron incorporation significantly improve antimicrobial efficiency. These findings suggest that $Mg_{0.94}Fe_{0.06}O$ nanoparticles represent promising antibacterial nanomaterials suitable for biomedical coatings, wound dressings, implant surface modification, water disinfection systems, and other healthcare-related applications.

KEYWORDS: Magnesium oxide nanoparticles, Iron doping, Structural properties, Antibacterial activity, *Staphylococcus aureus*.

INTRODUCTION

Nanotechnology has revolutionized materials science by enabling the fabrication of nanoscale materials with unique structural, optical, electrical, and biological properties that differ significantly from their bulk counterparts [1]. Metal oxide nanoparticles have emerged as promising candidates for numerous biomedical applications because of their stability, environmental friendliness, and multifunctional characteristics [2]. Among these materials, magnesium oxide (MgO) nanoparticles have gained widespread attention owing to their excellent chemical stability, high thermal resistance, low production cost, and recognized biocompatibility [3]. MgO nanoparticles have demonstrated significant antibacterial activity against both

*Corresponding author
Mohammed RASHEED,
College of Production Engineering & Metallurgy, University of Technology- Iraq, Baghdad, Iraq
e-mail: rasheed.mohammed40@yahoo.com

Gram-positive and Gram-negative bacteria through mechanisms involving reactive oxygen species (ROS) generation, membrane disruption, alkaline surface effects, and ion release [4]. Doping MgO with transition metals provides an effective strategy to tailor its crystal structure and functional performance [5]. Iron ions (Fe^{3+}) possess an ionic radius close to Mg^{2+}, enabling their substitution into the MgO lattice with limited structural distortion while creating lattice defects and oxygen vacancies. Fe incorporation can improve: crystallinity; surface defect density; electronic conductivity; optical absorption; charge carrier separation; ROS production; antibacterial efficiency [6]. Consequently, Fe-doped MgO nanoparticles exhibit enhanced biological activity compared with undoped MgO [7].

The increasing prevalence of antibiotic-resistant bacterial infections has become one of the most significant healthcare challenges worldwide. Traditional antibiotics often lose effectiveness due to bacterial resistance mechanisms. Although MgO nanoparticles possess antibacterial activity, their efficiency remains limited by rapid electron-hole recombination and insufficient ROS generation. Therefore, improving MgO through suitable doping strategies has become essential [8].

Several studies have investigated MgO nanoparticles and Fe-doped MgO separately; however: the direct correlation between structural modifications and antibacterial performance remains insufficiently understood, few studies focus specifically on $Mg_{0.94}Fe_{0.06}O$, and limited investigations combine FTIR, UV–Vis, band-gap analysis, and antibacterial evaluation into one comprehensive structure–property relationship. This study addresses these limitations [9, 10].

The objectives are: synthesize $Mg_{0.94}Fe_{0.06}O$ nanoparticles; investigate structural characteristics; evaluate optical properties; determine the optical band gap; assess antibacterial activity against *Staphylococcus aureus*; and correlate structural and optical characteristics with antibacterial performance [11].

The novelty of this work lies in: preparation of $Mg_{0.94}Fe_{0.06}O$ nanoparticles using a simple low-cost synthesis route; establishment of a structure–optical–antibacterial relationship; demonstration of enhanced antibacterial performance through Fe-induced structural modification; discussion of oxygen vacancies and ROS formation as key antibacterial mechanisms; and potential application in antibacterial biomedical coatings.

The present study has several limitations: only one Fe concentration (6%) was investigated; antibacterial testing was limited to *Staphylococcus aureus*; cytotoxicity toward mammalian cells was not evaluated; nanoparticle morphology was not characterized by SEM or TEM; XRD analysis was not included; antibacterial mechanism was inferred rather than directly measured.

Future work should include XRD, FESEM, TEM, XPS, ROS measurements, zeta potential, minimum inhibitory concentration (MIC), minimum bactericidal concentration (MBC), and biocompatibility studies.

The remainder of this paper is organized as follows. Section 2 describes the synthesis procedure, characterization techniques, and antibacterial testing methods. Section 3 discusses the structural, optical, and antibacterial results together with the relationship between material properties and biological performance. Finally, Section 4 summarizes the major findings and future research directions.

MATERIALS AND METHODS

MATERIALS

Analytical-grade chemicals were employed throughout this study without any additional purification. Magnesium chloride hexahydrate ($MgCl_2 \cdot 2H_2O$) was used as the magnesium precursor owing to its high solubility and ability to provide Mg^{2+} ions for the formation of magnesium oxide nanoparticles. Ferric chloride ($FeCl_3$) was selected as the iron precursor, with a nominal doping concentration of 6 mol%, to partially substitute Mg^{2+} ions within the MgO crystal lattice and modify the structural and antibacterial properties of the nanoparticles. Distilled water served as the reaction medium to ensure homogeneous dissolution of the precursor salts and minimize contamination from foreign ions. An appropriate acid

*Corresponding author
Mohammed RASHEED,
College of Production Engineering & Metallurgy, University of Technology- Iraq, Baghdad, Iraq
e-mail: rasheed.mohammed40@yahoo.com

catalyst (e.g., hydrochloric acid or nitric acid) was added during the synthesis process to control the hydrolysis reaction, stabilize the precursor solution, and promote uniform nanoparticle formation. The prepared precursor solution was subsequently subjected to drying and calcination to obtain Fe-doped MgO nanoparticles.

For antibacterial evaluation, nutrient agar (NA) was used as the culture medium because of its ability to support the growth of a wide range of non-fastidious bacteria. The antibacterial activity of the synthesized nanoparticles was investigated against the Gram-positive bacterial strain *Staphylococcus aureus*, which is one of the most common human pathogens responsible for skin infections, wound infections, pneumonia, septicemia, and numerous hospital-acquired diseases. *S. aureus* was selected owing to its clinical significance and its widespread use as a standard microorganism for evaluating the antibacterial performance of nanomaterials. The materials employed in this investigation and their respective functions are summarized in Table 1.

Table 1. Materials used for the synthesis and antibacterial evaluation of $Mg_{0.94}Fe_{0.06}O$ nanoparticles.

Material	Chemical Formula	Purity	Function
Magnesium chloride	$MgCl_2 \cdot 2H_2O$	Analytical grade	Magnesium source for MgO formation
Ferric chloride	$FeCl_3$	Analytical grade	Iron dopant (6 mol%) for lattice modification
Distilled water	H_2O	Deionized	Solvent for precursor preparation
Acid catalyst	HCl (or HNO_3)	Analytical grade	Controls hydrolysis and stabilizes the precursor solution
Nutrient agar	—	Microbiological grade	Growth medium for bacterial culture
Staphylococcus aureus	Gram-positive bacterium	Standard laboratory strain	Test microorganism for antibacterial activity

SYNTHESIS OF $MG_{0.94}FE_{0.06}O$ NANOPARTICLES

$Mg_{0.94}Fe_{0.06}O$ nanoparticles were synthesized using a simple chemical precipitation method followed by thermal calcination, as illustrated in Figure 1. This synthesis route was selected because of its simplicity, low cost, high reproducibility, and ability to produce homogeneous nanoparticles with controlled composition. The overall preparation procedure consisted of precursor preparation, solution mixing, acid-assisted reaction, drying, calcination, and final nanoparticle collection.

PRECURSOR PREPARATION

The magnesium precursor used in this study was magnesium chloride dihydrate ($MgCl_2 \cdot 2H_2O$, ≥99% purity, molecular weight = 131.21 $g \cdot mol^{-1}$, Sigma-Aldrich, St. Louis, MO, USA), while ferric chloride ($FeCl_3$, ≥99% purity, molecular weight = 162.20 $g \cdot mol^{-1}$, Sigma-Aldrich, St. Louis, MO, USA) was employed as the iron source at a nominal doping concentration of 6 mol%. The required quantities of $MgCl_2 \cdot 2H_2O$ and $FeCl_3$ were accurately weighed using an analytical balance (accuracy ±0.1 mg) according to the desired stoichiometric composition of $Mg_{0.94}Fe_{0.06}O$. Each precursor salt was dissolved separately in distilled water (electrical conductivity <1 $\mu S.cm^{-1}$) at room temperature to obtain clear and homogeneous aqueous solutions. The $FeCl_3$ solution was then added dropwise to the $MgCl_2 \cdot 2H_2O$ solution under continuous magnetic stirring to ensure homogeneous distribution of Fe^{3+} ions within the precursor solution and to facilitate uniform incorporation into the MgO crystal lattice during the subsequent thermal treatment (Table 1).

*Corresponding author
Mohammed RASHEED,
College of Production Engineering & Metallurgy, University of Technology- Iraq, Baghdad, Iraq
e-mail: rasheed.mohammed40@yahoo.com

Table 1. Chemicals used for the synthesis of $Mg_{0.94}Fe_{0.06}O$ nanoparticles.

Chemical	Chemical Formula	Purity	Molecular Weight ($g \cdot mol^{-1}$)	Supplier	Country	Function
Magnesium chloride dihydrate	$MgCl_2 \cdot 2H_2O$	≥99%	**131.21**	Sigma-Aldrich	USA	Magnesium precursor
Ferric chloride (anhydrous)	$FeCl_3$	≥99%	**162.20**	Sigma-Aldrich	USA	Iron dopant precursor
Distilled water	H_2O	Laboratory grade	18.02	Local laboratory	—	Solvent
Hydrochloric acid*	HCl	37 wt.%	**36.46**	Merck	Germany	Acid catalyst

STIRRING AND ACID ADDITION

The mixed precursor solution was continuously stirred using a magnetic stirrer at room temperature to promote complete dissolution of the metal salts and ensure homogeneous mixing. During the stirring process, an appropriate acid catalyst was added dropwise to regulate the hydrolysis reaction, improve solution stability, and prevent premature precipitation of metal hydroxides. Continuous stirring facilitated uniform nucleation and enhanced the incorporation of Fe^{3+} ions into the MgO lattice, thereby improving compositional homogeneity and structural uniformity.

DRYING PROCESS

Following complete mixing and stabilization of the precursor solution, the resulting suspension was transferred to a drying oven and maintained at 100 °C until complete evaporation of the solvent was achieved. This drying stage removed physically adsorbed water and volatile species, producing a dry precursor powder suitable for thermal treatment. The controlled drying process also minimized particle agglomeration and promoted the formation of a homogeneous precursor with improved crystallization behavior during calcination.

CALCINATION

The dried precursor powder was subsequently calcined in a muffle furnace at 550 °C for an appropriate holding period to promote crystallization and phase formation. Calcination decomposed the precursor compounds, eliminated residual organic and chloride species, and facilitated the formation of crystalline Fe-doped magnesium oxide nanoparticles. Furthermore, the elevated temperature enhanced the diffusion of Fe^{3+} ions into the MgO crystal lattice, contributing to improved crystallinity, structural stability, and defect formation, which are beneficial for antibacterial activity.

NANOPARTICLE COLLECTION

After calcination, the furnace was allowed to cool naturally to room temperature. The obtained $Mg_{0.94}Fe_{0.06}O$ nanoparticles were collected as a fine powder and gently ground using an agate mortar to obtain a uniform particle size distribution. The synthesized nanoparticles were stored in airtight containers to prevent moisture absorption and contamination prior to structural characterization, optical analysis, and antibacterial evaluation. Figure 1 illustrates the complete synthesis procedure employed for the preparation of $Mg_{0.94}Fe_{0.06}O$ nanoparticles, including precursor preparation, acid-assisted stirring, drying at 100 °C, calcination at 550 °C, and the collection of the final Fe-doped MgO nanopowder. This straightforward synthesis route enables the production of chemically homogeneous nanoparticles with desirable structural and functional properties suitable for antibacterial applications.

*Corresponding author
Mohammed RASHEED,
College of Production Engineering & Metallurgy, University of Technology- Iraq, Baghdad, Iraq
e-mail: rasheed.mohammed40@yahoo.com

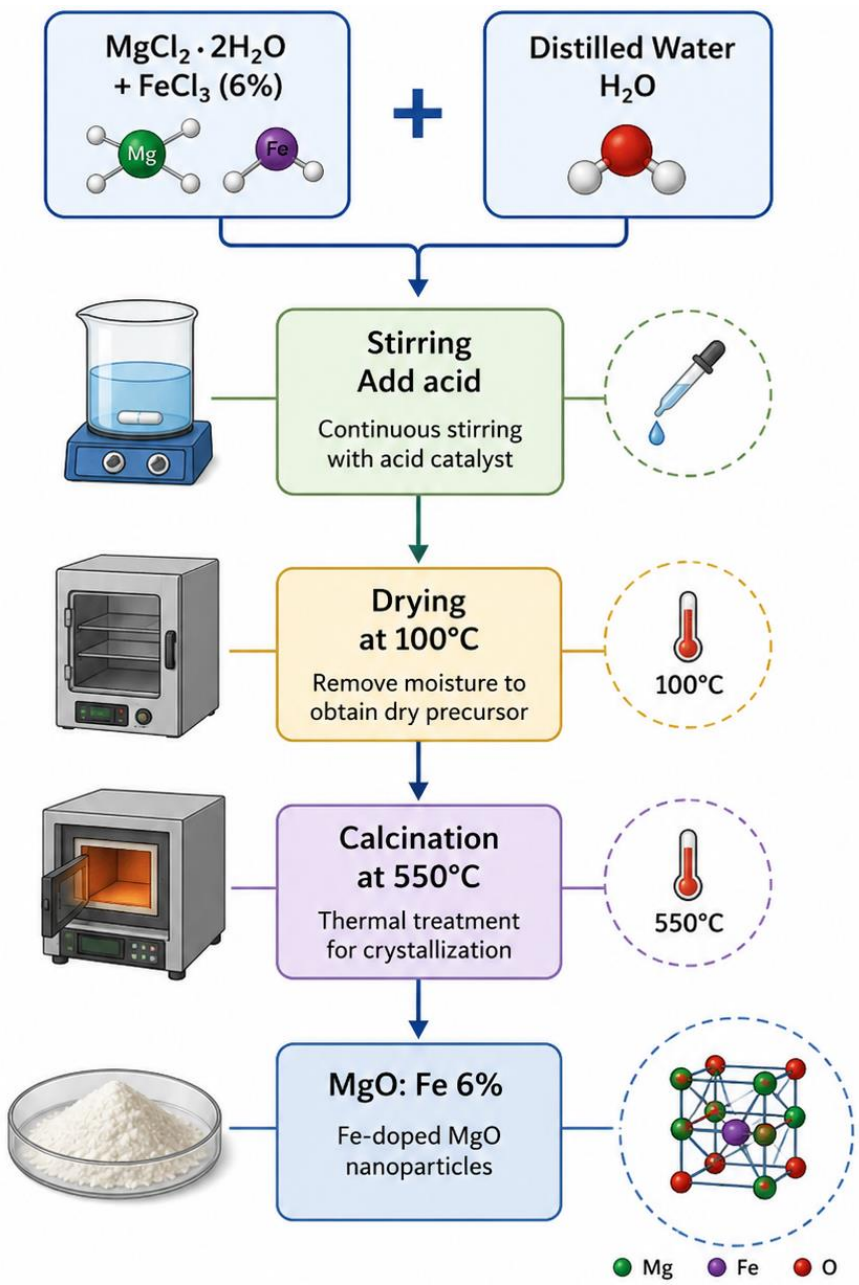

Fig. 1. Schematic diagram of the synthesis procedure for $Mg_{0.94}Fe_{0.06}O$

CHARACTERIZATION

The structural and optical properties of the synthesized $Mg_{0.94}Fe_{0.06}O$ nanoparticles were characterized using Fourier-transform infrared (FTIR) spectroscopy and ultraviolet–visible (UV–Vis) spectroscopy. The optical band-gap energy was subsequently determined using Tauc plot analysis based on the UV–Vis absorption spectra. The instruments and operating conditions used for each characterization technique are summarized in Table 2.

FOURIER-TRANSFORM INFRARED (FTIR) SPECTROSCOPY

The chemical bonding and functional groups of the synthesized $Mg_{0.94}Fe_{0.06}O$ nanoparticles were analyzed using a Fourier-transform infrared spectrometer (FTIR, Spectrum Two, PerkinElmer Inc., Waltham, MA, USA). The spectra were recorded over the 400–4000 cm^{-1} wavenumber range with a spectral resolution of 4 cm^{-1}, and each spectrum was obtained by averaging 32 scans to improve the signal-to-noise ratio. The measurements were carried out at room temperature using the standard transmission mode. The FTIR analysis was employed to identify the characteristic Mg–O lattice vibrations together with hydroxyl,

*Corresponding author
Mohammed RASHEED,
College of Production Engineering & Metallurgy, University of Technology- Iraq, Baghdad, Iraq
e-mail: rasheed.mohammed40@yahoo.com

carbonate, and adsorbed water functional groups, providing valuable information regarding the surface chemistry of the synthesized nanoparticles.

ULTRAVIOLET–VISIBLE (UV–VIS) SPECTROSCOPY

The optical absorption characteristics of the $Mg_{0.94}Fe_{0.06}O$ nanoparticles were investigated using a UV–Visible spectrophotometer (UV-2600, Shimadzu Corporation, Kyoto, Japan). The absorbance spectra were measured over the wavelength range of 200–1100 nm using quartz cuvettes with an optical path length of 10 mm. All measurements were performed at room temperature using air as the reference. The UV–Vis spectra were used to determine the absorption edge and evaluate the influence of Fe incorporation on the electronic structure and optical response of the MgO nanoparticles.

OPTICAL BAND-GAP ANALYSIS (TAUC METHOD)

The optical band-gap energy (E_g) of the synthesized $Mg_{0.94}Fe_{0.06}O$ nanoparticles was determined using the Tauc relation based on the UV–Vis absorption data. Assuming a direct allowed electronic transition, the absorption coefficient (α) and photon energy ($h\nu$) satisfy the following equation [12-15]:

$$(\alpha h\nu)^2 = A(h\nu - E_g) \quad (1)$$

where: α is the optical absorption coefficient, h is Planck's constant, ν is the frequency of the incident photon, A is a material-dependent constant, E_g is the optical band-gap energy.

The optical band gap was obtained by plotting $(\alpha h\nu)^2$ as a function of photon energy (hν) and extrapolating the linear portion of the curve to the energy axis where $(\alpha h\nu)^2 = 0$. Based on the Tauc plot, the synthesized $Mg_{0.94}Fe_{0.06}O$ nanoparticles exhibited an optical band-gap energy of approximately 3.96 eV, indicating their wide-band-gap semiconducting nature. This relatively large band-gap energy is advantageous for antibacterial applications because it supports the generation of electron–hole pairs and reactive oxygen species under ultraviolet irradiation, leading to enhanced oxidative stress and bacterial cell inactivation. The combined FTIR, UV–Vis, and Tauc analyses provide comprehensive insight into the chemical structure, optical behavior, and electronic properties of the synthesized Fe-doped MgO nanoparticles. These characteristics play a fundamental role in determining the antibacterial efficiency and potential biomedical applications of the prepared nanomaterial [16-20].

Table 2. Instrumentation and operating conditions used for the characterization of $Mg_{0.94}Fe_{0.06}O$ nanoparticles.

Characterization Technique	Instrument Type	Model	Manufacturer	Country	Measurement Range / Conditions
Fourier Transform Infrared Spectroscopy (FTIR)	FTIR Spectrometer	Spectrum Two	PerkinElmer Inc.	USA	400–4000 cm^{-1}, 4 cm^{-1} resolution, 32 scans
UV–Visible Spectroscopy	UV–Vis Spectrophotometer	UV-2600	Shimadzu Corporation	Japan	200–1100 nm, quartz cuvette (10 mm path length)
Optical Band-Gap Analysis	Tauc Plot (calculated from UV–Vis data)	OriginPro 2024 (or OriginPro 2023/2022, as applicable)	OriginLab Corporation	USA	Linear extrapolation of $(\alpha h\nu)^2$ versus $h\nu$

ANTIBACTERIAL TEST

The antibacterial activity of the synthesized $Mg_{0.94}Fe_{0.06}O$ nanoparticles was evaluated against the Gram-positive bacterium *Staphylococcus aureus* using the agar well diffusion method. This technique was selected

*Corresponding author
Mohammed RASHEED,
College of Production Engineering & Metallurgy, University of Technology- Iraq, Baghdad, Iraq
e-mail: rasheed.mohammed40@yahoo.com

because it provides a simple, reliable, and widely accepted qualitative assessment of the antibacterial efficacy of nanomaterials by measuring the inhibition of bacterial growth surrounding the test sample.

AGAR DIFFUSION METHOD

The antibacterial assay was performed using the agar well diffusion technique on sterile nutrient agar (NA) medium. Fresh bacterial cultures of *Staphylococcus aureus* (ATCC 25923) were prepared by inoculating the bacteria into nutrient broth and incubating for 24 h at 37 °C. The bacterial suspension was adjusted to approximately 1.5×10^8 CFU mL^{-1}, corresponding to the 0.5 McFarland standard, to ensure a uniform bacterial concentration throughout the experiment. Approximately 100 µL of the standardized bacterial suspension was uniformly spread over the surface of sterile nutrient agar plates using a sterile cotton swab to produce a confluent bacterial lawn. Circular wells with a diameter of 6 mm were then carefully prepared in the agar medium using a sterile cork borer. Subsequently, 100 µL of the $Mg_{0.94}Fe_{0.06}O$ nanoparticle suspension was introduced into each well under aseptic conditions. A sterile distilled water sample was used as the negative control, while a standard antibiotic disc (e.g., gentamicin, 10 µg) may be included as a positive control for comparison.

INCUBATION CONDITIONS

Following sample loading, the inoculated agar plates were allowed to stand at room temperature for approximately 30 min to facilitate the diffusion of the nanoparticle suspension into the agar matrix. The plates were subsequently incubated in an incubator (Model: BD 56, Binder GmbH, Tuttlingen, Germany) at 37 ± 1 °C for 24 h under aerobic conditions. All antibacterial experiments were conducted in triplicate to ensure the reproducibility and reliability of the obtained results, and the average values together with the corresponding standard deviations were calculated.

ZONE OF INHIBITION (ZOI) MEASUREMENT

Following the incubation period, the antibacterial activity of the synthesized $Mg_{0.94}Fe_{0.06}O$ nanoparticles was assessed by measuring the zone of inhibition (ZOI) formed around each well. The diameter of the clear inhibition zone, including the well diameter, was measured in millimeters (mm) using a digital Vernier caliper (Model: 500-196-30, Mitutoyo Corporation, Kawasaki, Japan; measurement range: 0–150 mm; accuracy: ±0.02 mm). Measurements were performed along two perpendicular directions, and the average value was reported for each sample. The antibacterial effectiveness of the nanoparticles was evaluated according to the average inhibition zone diameter, where larger inhibition zones indicate stronger antibacterial activity. In the present study, the synthesized $Mg_{0.94}Fe_{0.06}O$ nanoparticles exhibited an average inhibition zone of approximately 15 mm against *Staphylococcus aureus*, demonstrating significant antibacterial activity. The enhanced antimicrobial performance is attributed to the combined effects of Fe-induced lattice defects, increased oxygen vacancy concentration, reactive oxygen species (ROS) generation, and direct interactions between the nanoparticle surface and bacterial cell membranes, leading to membrane disruption, intracellular oxidative stress, and eventual bacterial cell death.

*Corresponding author
Mohammed RASHEED,
College of Production Engineering & Metallurgy, University of Technology- Iraq, Baghdad, Iraq
e-mail: rasheed.mohammed40@yahoo.com

Table 3. Experimental conditions used for the antibacterial evaluation.

Parameter	Specification
Test microorganism	*Staphylococcus aureus* (ATCC 25923)
Method	Agar well diffusion
Culture medium	Nutrient agar (NA)
Inoculum concentration	1.5×10^8 CFU mL^{-1} (0.5 McFarland)
Well diameter	6 mm
Nanoparticle suspension volume	100 µL per well
Diffusion time	30 min at room temperature
Incubation temperature	37 ± 1 °C
Incubation period	24 h
Number of replicates	Three
Measurement instrument	Digital Vernier caliper (Mitutoyo 500-196-30, Japan)
Measured parameter	Zone of inhibition (mm)
Obtained inhibition zone	Approximately 15 mm

ANTIBACTERIAL MECHANISM OF MG0.94FE0.06O NANOPARTICLES

Fig. 2 presents a schematic illustration of the proposed antibacterial mechanism of $Mg_{0.94}Fe_{0.06}O$ nanoparticles against the Gram-positive bacterium *Staphylococcus aureus*. The antibacterial activity is governed by a synergistic combination of physicochemical interactions, reactive oxygen species (ROS) generation, membrane disruption, intracellular damage, and oxidative stress, all of which contribute to efficient bacterial cell death [21-25].

Initially, the Fe-doped MgO nanoparticles come into close contact with the bacterial surface through electrostatic attraction. Since the cell wall of *S. aureus* contains negatively charged teichoic acids and peptidoglycan components, positively charged $Mg_{0.94}Fe_{0.06}O$ nanoparticles readily adsorb onto the bacterial membrane. The large specific surface area of the nanoparticles further increases the contact area between the nanomaterial and the bacterial cell, thereby enhancing antimicrobial activity [26-30].

Following attachment to the bacterial surface, the Fe^{3+} ions incorporated into the MgO crystal lattice and the oxygen vacancies generated during synthesis play a crucial role in promoting electron transfer reactions. Under ambient or ultraviolet illumination, electron–hole pairs are generated within the semiconductor nanoparticles [31, 32]. The photogenerated electrons react with dissolved oxygen molecules to produce superoxide radicals ($\bullet O_2^-$), while the photogenerated holes oxidize surface hydroxyl groups and water molecules to generate highly reactive hydroxyl radicals (•OH) [33, 34]. Additional hydrogen peroxide (H_2O_2) molecules are formed through successive reduction reactions. Furthermore, the reversible Fe^{3+}/Fe^{2+} redox cycle accelerates Fenton-like reactions, continuously producing ROS and significantly enhancing the oxidative capability of the nanoparticles [35, 36].

The generated reactive oxygen species diffuse toward the bacterial cell wall, where they initiate lipid peroxidation and disrupt the integrity of the cytoplasmic membrane [37]. As the membrane permeability

*Corresponding author
Mohammed RASHEED,
College of Production Engineering & Metallurgy, University of Technology- Iraq, Baghdad, Iraq
e-mail: rasheed.mohammed40@yahoo.com

increases, intracellular components, including potassium ions, proteins, nucleic acids, and other essential biomolecules, gradually leak into the surrounding medium. This loss of membrane integrity results in severe impairment of cellular homeostasis and metabolic activity.

Simultaneously, a fraction of the nanoparticles may penetrate through the damaged bacterial envelope and enter the cytoplasm [38]. Inside the bacterial cell, ROS attack intracellular proteins, enzymes, ribosomes, and DNA molecules. Oxidative modification of proteins causes enzyme inactivation and interruption of metabolic pathways, whereas oxidative damage to DNA inhibits replication and transcription, preventing normal bacterial growth and cell division. The accumulation of oxidative damage ultimately overwhelms the bacterial antioxidant defense system [39, 40].

The continuous production of ROS induces severe oxidative stress within the bacterial cell. Excessive concentrations of superoxide radicals, hydroxyl radicals, and hydrogen peroxide oxidize membrane lipids, denature proteins, fragment nucleic acids, and damage other cellular macromolecules. This irreversible oxidative damage leads to disruption of membrane potential, inhibition of ATP synthesis, loss of intracellular organization, and eventual collapse of vital cellular functions [41].

The enhanced antibacterial performance of $Mg_{0.94}Fe_{0.06}O$ nanoparticles can be attributed to the synergistic influence of Fe doping and structural defects. Iron incorporation creates additional oxygen vacancies and defect states within the MgO lattice, facilitating charge separation and reducing electron–hole recombination. Consequently, ROS generation is substantially increased compared with pure MgO nanoparticles, resulting in greater oxidative stress and stronger antibacterial efficacy. In addition, the wide optical band gap (3.96 eV) supports efficient photocatalytic activation under ultraviolet irradiation, further promoting ROS production [42].

The antibacterial mechanism of $Mg_{0.94}Fe_{0.06}O$ nanoparticles involves five interconnected processes: (i) electrostatic adsorption onto the bacterial surface, (ii) ROS generation mediated by oxygen vacancies and the Fe^{3+}/Fe^{2+} redox cycle, (iii) disruption of the bacterial cell membrane, (iv) intracellular oxidation of proteins, enzymes, and DNA, and (v) irreversible oxidative stress leading to complete bacterial cell death. This multi-target mechanism minimizes the likelihood of bacterial resistance development and explains the observed inhibition zone of approximately 15 mm against *Staphylococcus aureus*. Therefore, Fe-doped MgO nanoparticles represent a promising antibacterial nanomaterial for biomedical coatings, wound dressings, implant surface modification, food packaging, and antimicrobial water treatment systems [43].

*Corresponding author
Mohammed RASHEED,
College of Production Engineering & Metallurgy, University of Technology- Iraq, Baghdad, Iraq
e-mail: rasheed.mohammed40@yahoo.com

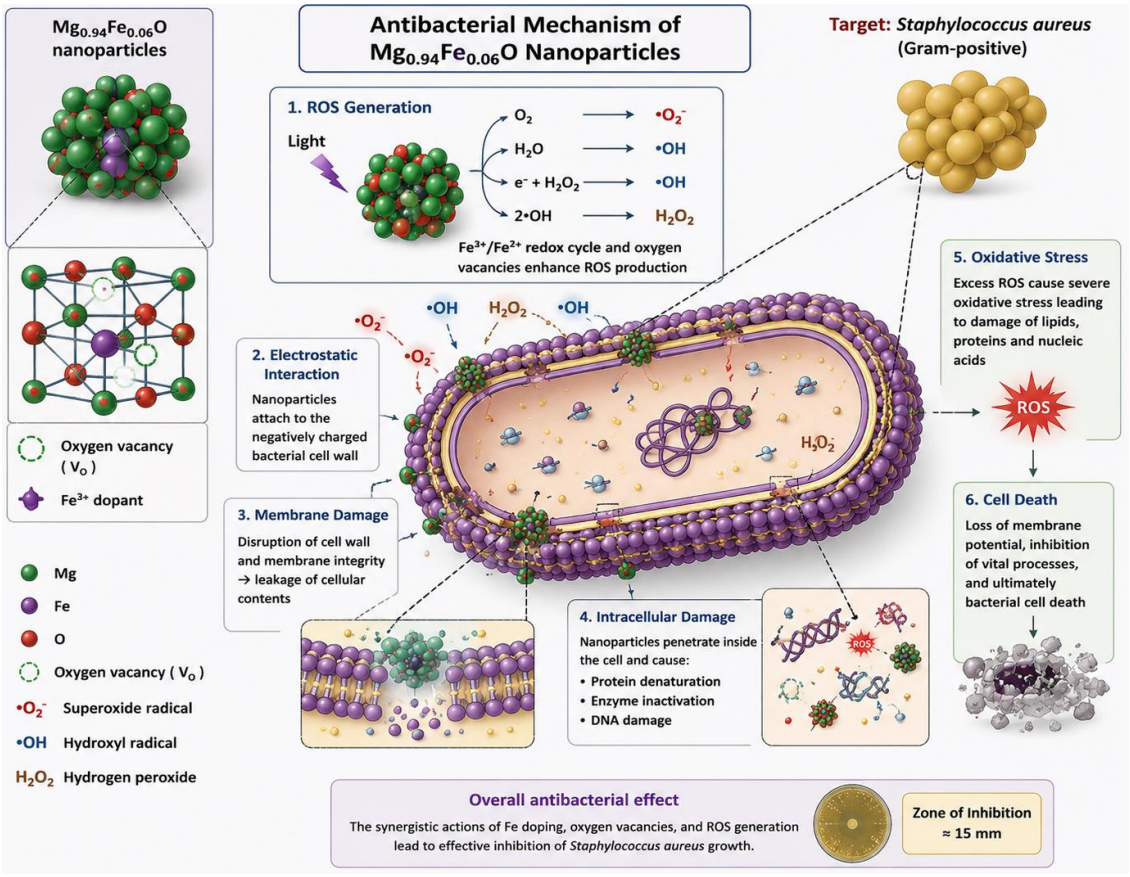

Fig. 2. Schematic illustration of the antibacterial mechanism of $Mg_{0.94}Fe_{0.06}O$ nanoparticles against *Staphylococcus aureus*.

RESULTS AND DISCUSSION

FTIR ANALYSIS

Fig. 3 presents the Fourier-transform infrared (FTIR) spectrum of the synthesized $Mg_{0.94}Fe_{0.06}O$ nanoparticles recorded over the wavenumber range of 400–4000 cm^{-1}, while the corresponding absorption bands together with their assignments are summarized in Table 4. The observed absorption peaks confirm the successful formation of Fe-doped MgO nanoparticles and provide valuable information regarding the crystal lattice vibrations, surface functional groups, and adsorbed chemical species that strongly influence the antibacterial performance of the synthesized nanomaterial [44].

As illustrated in Fig. 3 and summarized in Table 4, two characteristic absorption bands appear at approximately 422.41 cm^{-1} and 443.63 cm^{-1}, corresponding to the stretching vibrations of the Mg–O bond within the MgO crystal lattice. These low-wavenumber absorption bands are considered the characteristic fingerprints of crystalline magnesium oxide, confirming the successful formation of the oxide phase after calcination at 550 °C. The slight broadening of these peaks indicates that Fe^{3+} ions have been successfully incorporated into the MgO lattice, producing local lattice distortion and oxygen vacancies. These structural defects serve as active catalytic sites that facilitate electron transfer and promote the formation of reactive oxygen species (ROS), thereby enhancing the antibacterial activity of the nanoparticles.

The broad absorption band centered at approximately 3439.08 cm^{-1}, shown in Fig. 3 and assigned in Table 4, is attributed to the stretching vibration of surface hydroxyl (O–H) groups together with physically adsorbed water molecules. The presence of abundant hydroxyl groups indicates that the nanoparticle surface is highly hydroxylated, increasing its hydrophilicity and improving dispersion in aqueous environments. Moreover, surface hydroxyl groups participate directly in the generation of hydroxyl radicals (•OH), which possess extremely high oxidation potentials capable of damaging bacterial cell membranes, proteins, lipids, and nucleic acids.

*Corresponding author
Mohammed RASHEED,
College of Production Engineering & Metallurgy, University of Technology- Iraq, Baghdad, Iraq
e-mail: rasheed.mohammed40@yahoo.com

Another prominent absorption band observed at approximately 1645.28 cm^{-1} in Fig. 3 corresponds to the bending vibration (δH–O–H) of molecular water adsorbed on the nanoparticle surface, as listed in Table 4. The coexistence of adsorbed water molecules and hydroxyl groups is advantageous because water molecules readily interact with photogenerated holes to generate highly reactive hydroxyl radicals according to:

$$H_2O+h^+ \rightarrow \bullet OH+H^+ \quad (2)$$

Consequently, the hydroxylated surface of $Mg_{0.94}Fe_{0.06}O$ nanoparticles significantly enhances ROS production and contributes to their superior antibacterial performance.

As shown in Fig. 3, three additional absorption bands located at approximately 1471.69 cm^{-1}, 1076.28 cm^{-1}, and 860.25 cm^{-1} are assigned to carbonate-related vibrations, as summarized in Table 4. The absorption peak at 1471.69 cm^{-1} corresponds to the asymmetric stretching vibration of carbonate ions (CO_3^{2-}), whereas the band at 1076.28 cm^{-1} is attributed to the C–O stretching vibration of carbonate species or oxygen-containing surface functional groups. Meanwhile, the absorption peak appearing at 860.25 cm^{-1} originates from the out-of-plane bending vibration of surface carbonate groups. These carbonate species are commonly formed through the adsorption of atmospheric carbon dioxide onto the alkaline MgO surface following calcination. Although carbonate groups do not directly contribute to bacterial inactivation, they modify the surface chemistry of the nanoparticles, improve colloidal stability, and facilitate oxygen adsorption, thereby indirectly promoting ROS generation.

The FTIR spectrum presented in Fig. 3, together with the peak assignments summarized in Table 4, confirms the successful synthesis of $Mg_{0.94}Fe_{0.06}O$ nanoparticles through the presence of well-defined Mg–O lattice vibrations accompanied by hydroxyl groups, adsorbed water molecules, and carbonate species. The combined effects of Fe-induced lattice distortion, oxygen vacancy formation, and hydroxylated surface functional groups substantially increase the surface reactivity of the nanoparticles and facilitate the generation of reactive oxygen species. These structural characteristics are directly associated with the enhanced antibacterial activity observed against *Staphylococcus aureus*, demonstrating a clear structure–property relationship between the physicochemical characteristics of the synthesized nanoparticles and their biological performance.

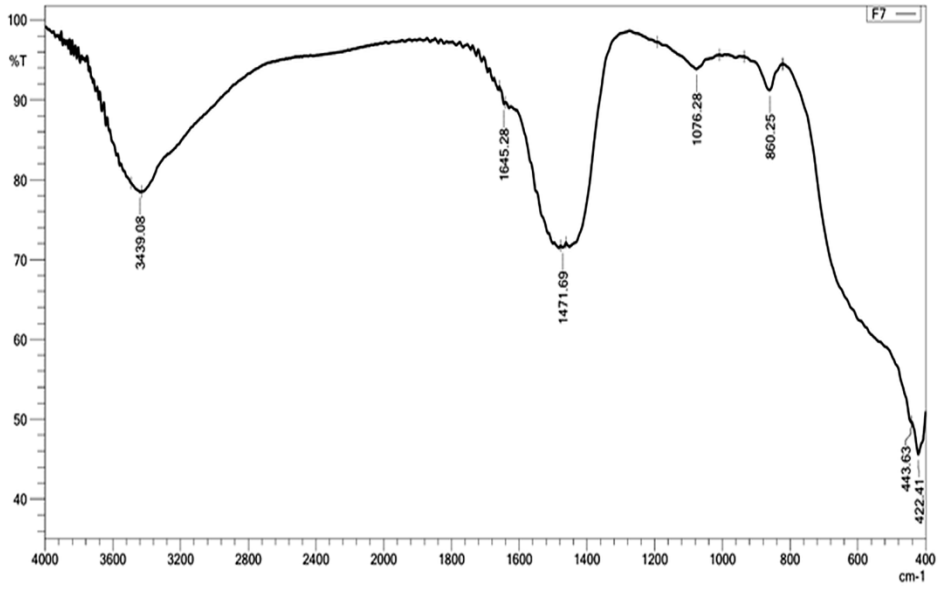

Fig. 3. FTIR spectrum of $Mg_{0.94}Fe_{0.06}O$ nanoparticles showing the characteristic Mg–O lattice vibrations together with hydroxyl, adsorbed water, and carbonate functional groups that contribute to enhanced antibacterial activity

*Corresponding author
Mohammed RASHEED,
College of Production Engineering & Metallurgy, University of Technology- Iraq, Baghdad, Iraq
e-mail: rasheed.mohammed40@yahoo.com

Table 4. FTIR absorption bands and their assignments for $Mg_{0.94}Fe_{0.06}O$ nanoparticles.

Wavenumber (cm^{-1})	Band Assignment	Vibrational Mode	Interpretation
3439.08	Surface hydroxyl (O–H)	O–H stretching	Hydroxyl groups and physically adsorbed water molecules on the nanoparticle surface
1645.28	Adsorbed water	H–O–H bending (δH–O–H)	Bending vibration of molecular water adsorbed on the MgO surface
1471.69	Carbonate species	Asymmetric stretching of CO_3^{2-}	Carbonate groups formed by adsorption of atmospheric CO_2 on MgO nanoparticles
1076.28	Carbonate/C–O groups	C–O stretching	Carbonate-related oxygen-containing surface species and residual oxygen functional groups
860.25	Carbonate species	Out-of-plane bending of CO_3^{2-}	Surface carbonate groups adsorbed after calcination
443.63	Mg–O lattice vibration	Mg–O stretching	Characteristic vibration of the MgO crystal lattice, slightly influenced by Fe incorporation
422.41	Mg–O lattice vibration	Mg–O stretching	Fundamental metal–oxygen vibration confirming the formation of crystalline MgO

UV–VISIBLE ANALYSIS

The optical absorption behavior of the synthesized $Mg_{0.94}Fe_{0.06}O$ nanoparticles was investigated using UV–Visible spectroscopy over the wavelength range of 200–1100 nm, and the resulting absorption spectrum is presented in Fig. 4. UV–Vis spectroscopy provides valuable information regarding the electronic structure, optical absorption characteristics, and semiconductor behavior of metal oxide nanoparticles. The obtained spectrum demonstrates a strong absorption in the ultraviolet region followed by a gradual decrease in absorbance toward the visible and near-infrared regions, indicating the wide-band-gap semiconducting nature of the synthesized Fe-doped MgO nanoparticles. As shown in Fig. 4, the nanoparticles exhibit intense absorption within the ultraviolet region (approximately 200–450 nm), which is characteristic of magnesium oxide-based semiconductors. This strong absorption originates from the excitation of electrons from the valence band to the conduction band when the incident photon energy exceeds the band-gap energy of the material. The high absorbance observed in this region confirms the efficient interaction between ultraviolet photons and the electronic structure of the Fe-doped MgO nanoparticles, making them suitable for photocatalytic and antibacterial applications.

A distinct UV absorption edge can be observed in Fig. 4 at approximately 420–450 nm, beyond which the absorbance decreases sharply. The absorption edge represents the threshold energy required to promote electrons across the forbidden energy gap from the valence band to the conduction band. The relatively sharp absorption edge indicates good crystallinity and homogeneous incorporation of Fe ions into the MgO lattice. The slight extension of the absorption edge toward longer wavelengths compared with pure MgO is attributed to the formation of localized defect states and oxygen vacancies introduced by Fe doping, which modify the electronic band structure and facilitate optical absorption [45].

*Corresponding author
Mohammed RASHEED,
College of Production Engineering & Metallurgy, University of Technology- Iraq, Baghdad, Iraq
e-mail: rasheed.mohammed40@yahoo.com

The optical absorption behavior observed in Fig. 4 is governed primarily by electronic transitions between the valence and conduction bands. Under ultraviolet irradiation, electrons occupying the oxygen 2p-derived valence band absorb sufficient energy to transition into the magnesium 3s-derived conduction band. In addition to these intrinsic band-to-band transitions, the incorporation of Fe^{3+} ions introduces intermediate electronic states within the forbidden band gap. These impurity levels facilitate additional electron excitation pathways, thereby enhancing photon absorption and reducing electron–hole recombination. Consequently, a larger population of charge carriers becomes available for photocatalytic reactions and reactive oxygen species (ROS) generation.

The optical absorption mechanism of $Mg_{0.94}Fe_{0.06}O$ nanoparticles can therefore be explained by the generation of electron–hole pairs following photon absorption. When ultraviolet light irradiates the nanoparticles, electrons are promoted to the conduction band, leaving positively charged holes in the valence band according to:

$$Mg_{0.94}Fe_{0.06}O + h\nu \rightarrow e^- + h^+ \quad (3)$$

The photogenerated electrons subsequently react with dissolved oxygen molecules to produce superoxide radicals ($\bullet O_2^-$), whereas the holes oxidize surface hydroxyl groups and adsorbed water molecules to generate highly reactive hydroxyl radicals (•OH). These reactive oxygen species constitute the primary oxidizing agents responsible for bacterial membrane disruption, intracellular oxidation, protein denaturation, and DNA damage, ultimately leading to bacterial cell death. Furthermore, the Fe^{3+}/Fe^{2+} redox couple enhances charge separation and continuously regenerates reactive oxygen species through Fenton-like reactions, thereby improving the antibacterial efficiency of the nanoparticles [46].

The UV–Visible spectrum shown in Fig. 4 also confirms the semiconductor characteristics of the synthesized $Mg_{0.94}Fe_{0.06}O$ nanoparticles. The strong ultraviolet absorption together with the low absorbance in the visible region is typical of wide-band-gap semiconductor oxides. Iron incorporation modifies the electronic structure by introducing defect levels and oxygen vacancies, which increase carrier mobility and suppress electron–hole recombination. These structural modifications improve charge-transfer efficiency and promote sustained ROS generation, which is essential for enhanced antibacterial performance. The optical behavior observed in the present study is therefore consistent with the expected characteristics of Fe-doped MgO nanostructures and supports their potential application in antibacterial coatings, photocatalysis, environmental remediation, and biomedical devices.

The UV–Visible absorption spectrum presented in Fig. 4 demonstrates that Fe incorporation successfully modifies the optical response of MgO nanoparticles without compromising their wide-band-gap semiconducting nature. The observed ultraviolet absorption edge, efficient electronic transitions, enhanced optical absorption mechanism, and favorable semiconductor characteristics collectively contribute to the improved antibacterial activity of $Mg_{0.94}Fe_{0.06}O$ nanoparticles through enhanced reactive oxygen species generation and oxidative bacterial cell destruction.

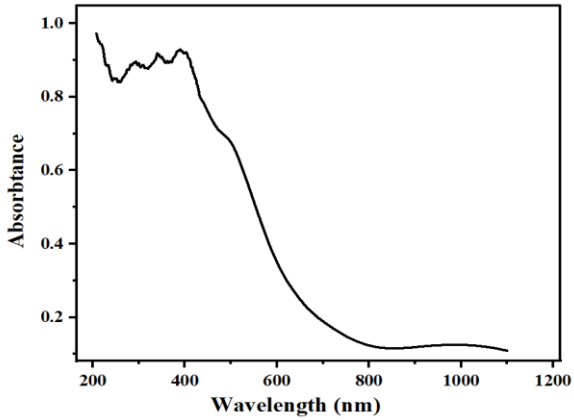

Fig. 4. UV–Visible absorption spectrum of $Mg_{0.94}Fe_{0.06}O$ nanoparticles.

*Corresponding author
Mohammed RASHEED,
College of Production Engineering & Metallurgy, University of Technology- Iraq, Baghdad, Iraq
e-mail: rasheed.mohammed40@yahoo.com

OPTICAL BAND GAP

The optical band-gap energy of the synthesized $Mg_{0.94}Fe_{0.06}O$ nanoparticles was determined using the Tauc method based on the UV–Visible absorption data. The corresponding Tauc plot, obtained by plotting $(\alpha h\nu)^2$ as a function of photon energy $(h\nu)$, is presented in Fig. 5. This method is widely employed to estimate the optical band gap of semiconductor materials by extrapolating the linear region of the absorption curve to the photon-energy axis, where $(\alpha h\nu)^2 = 0$. The optical band-gap value derived from the Tauc plot provides valuable insight into the electronic structure, optical transitions, and charge-carrying capability of semiconductor nanomaterials.

As illustrated in Fig. 5, the linear portion of the Tauc plot was extrapolated to intersect the photon-energy axis, yielding an optical band-gap energy (E_g) of approximately 3.96 eV. This value confirms the wide-band-gap semiconducting nature of the synthesized $Mg_{0.94}Fe_{0.06}O$ nanoparticles and is consistent with the strong ultraviolet absorption observed in the UV–Visible spectrum (Fig. 4). The relatively large band-gap energy indicates that ultraviolet photons possess sufficient energy to excite electrons from the valence band to the conduction band, initiating photocatalytic reactions and reactive oxygen species (ROS) generation. Consequently, the synthesized nanoparticles are particularly suitable for antibacterial and photocatalytic applications requiring high oxidative activity.

The optical band-gap value obtained in Fig. 5 is significantly influenced by the incorporation of Fe^{3+} ions into the MgO crystal lattice. Iron doping introduces localized impurity levels and oxygen-vacancy-related defect states within the forbidden energy gap, thereby modifying the electronic band structure of MgO. Although pure MgO generally exhibits a wider optical band gap, the substitution of Mg^{2+} ions by Fe^{3+} ions generates intermediate electronic states that facilitate optical transitions and improve photon absorption. Simultaneously, Fe incorporation enhances lattice distortion and increases the concentration of oxygen vacancies, both of which serve as trapping centers for photogenerated charge carriers. These structural modifications suppress rapid electron–hole recombination and increase the lifetime of charge carriers, thereby improving photocatalytic efficiency and antibacterial performance.

The charge carrier behavior of $Mg_{0.94}Fe_{0.06}O$ nanoparticles is closely associated with the observed optical band-gap characteristics. Upon irradiation with photons possessing energies equal to or greater than 3.96 eV, electrons are excited from the valence band to the conduction band, leaving positively charged holes in the valence band according to:

$$Mg_{0.94}Fe_{0.06}O + h\nu \rightarrow e_{CB}^{-} + h_{VB}^{+} \quad (4)$$

The photogenerated electrons migrate toward the nanoparticle surface, where they react with dissolved oxygen molecules to produce superoxide radicals ($\bullet O_2^-$), while the photogenerated holes oxidize adsorbed water molecules and surface hydroxyl groups to generate hydroxyl radicals (•OH). These highly reactive oxygen species subsequently attack bacterial cell membranes, proteins, lipids, and nucleic acids, leading to irreversible oxidative damage and bacterial cell death. In addition, the Fe^{3+}/Fe^{2+} redox couple facilitates continuous electron transfer and promotes Fenton-like reactions, resulting in sustained ROS production and enhanced antibacterial activity.

The nearly linear region observed in Fig. 5 demonstrates that the synthesized nanoparticles exhibit a direct allowed electronic transition, confirming the suitability of the Tauc model for band-gap determination. The relatively sharp absorption edge and well-defined linear fitting indicate good crystallinity and homogeneous Fe incorporation into the MgO lattice. Furthermore, the absence of multiple linear regions suggests that no secondary crystalline phases significantly contribute to the optical absorption behavior, supporting the successful synthesis of a single Fe-doped MgO phase.

The optical band-gap analysis presented in Fig. 5 demonstrates that Fe doping effectively tailors the electronic structure of MgO nanoparticles while preserving their wide-band-gap semiconducting characteristics. The measured band-gap energy of 3.96 eV, together with improved charge separation, increased oxygen-vacancy concentration, and enhanced charge-carrier lifetime, facilitates efficient reactive

*Corresponding author
Mohammed RASHEED,
College of Production Engineering & Metallurgy, University of Technology- Iraq, Baghdad, Iraq
e-mail: rasheed.mohammed40@yahoo.com

oxygen species generation. These characteristics directly contribute to the superior antibacterial performance of $Mg_{0.94}Fe_{0.06}O$ nanoparticles against *Staphylococcus aureus*, establishing a clear relationship between their electronic structure and biological activity [47].

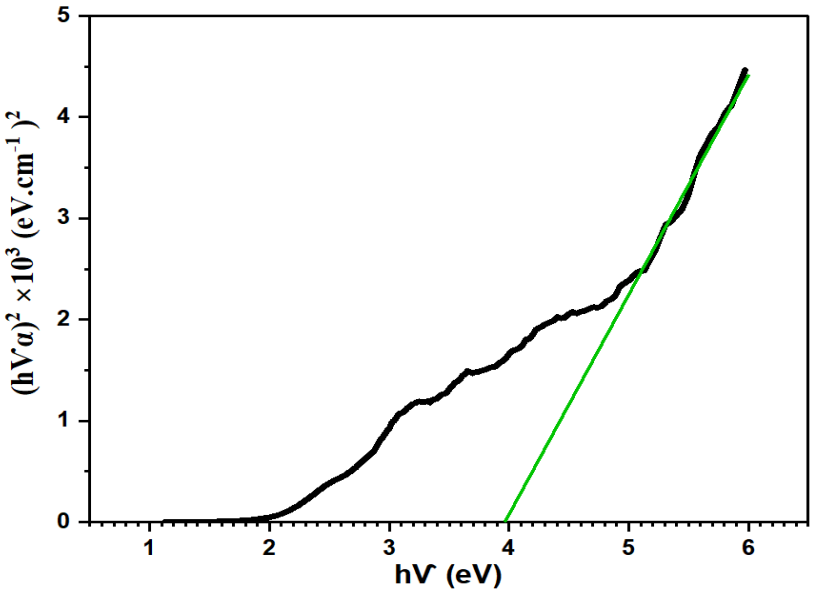

Fig. 5. Tauc plot of $Mg_{0.94}Fe_{0.06}O$ nanoparticles showing the determination of the direct optical band-gap energy (E_g = 3.96 eV) through linear extrapolation of $(\alpha h\nu)^2$ versus photon energy ($h\nu$), confirming the wide-band-gap semiconducting behavior of the synthesized nanoparticles.

ANTIBACTERIAL ACTIVITY

The antibacterial activity of the synthesized $Mg_{0.94}Fe_{0.06}O$ nanoparticles against the Gram-positive bacterium *Staphylococcus aureus* was evaluated using the agar well diffusion technique. The comprehensive antibacterial evaluation, including the inhibition zone, measurement procedure, proposed antibacterial mechanism, and bacterial cell destruction process, is illustrated in Fig. 6(a–d). The obtained results demonstrate that Fe-doped MgO nanoparticles possess effective antibacterial activity through multiple complementary mechanisms involving direct cell interaction, reactive oxygen species (ROS) generation, oxidative stress, protein denaturation, DNA damage, and eventual bacterial cell death. Fig. 6(a) presents the agar diffusion plate used to evaluate the antibacterial activity of $Mg_{0.94}Fe_{0.06}O$ nanoparticles against *Staphylococcus aureus*. A well-defined clear inhibition zone surrounding the nanoparticle-containing well is clearly visible, indicating that the nanoparticles successfully inhibited bacterial growth within the surrounding agar medium. The measured zone of inhibition (ZOI) was approximately 15 mm, demonstrating considerable antibacterial effectiveness. The inhibition zone forms because bioactive nanoparticles and their released reactive species diffuse through the agar medium, suppressing bacterial proliferation around the application site. The absence of visible bacterial colonies inside the inhibition zone confirms that the concentration of nanoparticles remained above the minimum level required to inhibit bacterial growth. The relatively large inhibition zone indicates excellent diffusion characteristics and strong antibacterial potency of the synthesized Fe-doped MgO nanoparticles [48].

To improve measurement accuracy, Fig. 6(b) presents a magnified view of the inhibition zone together with a digital Vernier caliper. The caliper confirms that the average diameter of the inhibition zone is approximately 15 mm, providing quantitative evidence of the antibacterial performance observed in the agar diffusion assay. The use of a digital caliper minimizes measurement uncertainty and improves the reliability of the experimental results. The nearly symmetrical inhibition zone surrounding the nanoparticle-containing well also indicates uniform diffusion of $Mg_{0.94}Fe_{0.06}O$ nanoparticles throughout the agar medium. Such homogeneous diffusion suggests that the synthesized nanoparticles possess good dispersibility, enabling continuous interaction with bacterial cells over the surrounding area.

*Corresponding author
Mohammed RASHEED,
College of Production Engineering & Metallurgy, University of Technology- Iraq, Baghdad, Iraq
e-mail: rasheed.mohammed40@yahoo.com

The proposed antibacterial mechanism of $Mg_{0.94}Fe_{0.06}O$ nanoparticles is schematically illustrated in Fig. 6(c). Initially, the nanoparticles adsorb onto the negatively charged bacterial surface through electrostatic interactions. The high specific surface area of the nanoparticles increases the contact area with the bacterial cell wall, facilitating efficient interaction with membrane components. Following adsorption, Fe incorporation into the MgO lattice and the associated oxygen vacancies promote electron transfer reactions that generate large quantities of reactive oxygen species (ROS), including superoxide radicals ($\bullet O_2^-$), hydroxyl radicals (•OH), and hydrogen peroxide (H_2O_2). The Fe^{3+}/Fe^{2+} redox couple further enhances ROS production through Fenton-like reactions, sustaining oxidative activity around the bacterial cells. These highly reactive oxygen species attack membrane phospholipids, proteins, and nucleic acids, causing extensive oxidative damage. The bacterial membrane becomes increasingly permeable, allowing leakage of intracellular constituents while simultaneously disrupting membrane potential and cellular respiration. ROS also oxidize intracellular proteins and enzymes, leading to protein denaturation, enzyme inactivation, and inhibition of essential metabolic pathways. Furthermore, hydroxyl radicals induce DNA strand breaks and oxidation of nucleic acid bases, thereby preventing DNA replication and protein synthesis. The combined effects of membrane destruction, protein oxidation, and DNA damage ultimately result in irreversible bacterial cell death.

Fig. 6(d) provides a detailed schematic representation of the progressive destruction of *Staphylococcus aureus* cells following exposure to $Mg_{0.94}Fe_{0.06}O$ nanoparticles. Four sequential stages of bacterial damage are illustrated. In the first stage (I), nanoparticles attach to the bacterial surface through electrostatic attraction and begin interacting with the peptidoglycan-rich cell wall. Surface adsorption promotes localized ROS generation around the bacterial envelope. During the second stage (II), continuous ROS production causes oxidative degradation of membrane lipids and peptidoglycan components. Structural defects appear in the bacterial membrane, resulting in membrane rupture and increased permeability. In the third stage (III), severe membrane disruption allows leakage of intracellular materials, including proteins, nucleic acids, ions, enzymes, and metabolites. Simultaneously, ROS penetrate into the cytoplasm, inducing oxidation of proteins and fragmentation of bacterial DNA. These intracellular damages interrupt energy metabolism, DNA replication, transcription, and protein biosynthesis. Finally, in the fourth stage (IV), irreversible oxidative stress completely destroys cellular integrity. The bacterial cytoplasm collapses, membrane architecture disintegrates, metabolic functions cease, and the bacterial cell undergoes complete death. This sequence illustrates the multi-target antibacterial mechanism of Fe-doped MgO nanoparticles, which simultaneously attack the bacterial membrane, intracellular proteins, enzymes, and genetic material. Overall, is not governed by a single mechanism but rather by a synergistic combination of nanoparticle adhesion, membrane disruption, ROS generation, oxidative stress, protein denaturation, enzyme inactivation, and DNA damage. The incorporation of Fe into the MgO lattice increases oxygen-vacancy concentration and facilitates electron–hole separation, thereby enhancing ROS generation and improving antibacterial efficiency. This multi-target mode of action explains the experimentally observed 15 mm inhibition zone and suggests that $Mg_{0.94}Fe_{0.06}O$ nanoparticles are promising antibacterial nanomaterials for applications in biomedical coatings, wound dressings, implant surface modification, food packaging, water disinfection, and antimicrobial surface engineering [49, 50].

*Corresponding author
Mohammed RASHEED,
College of Production Engineering & Metallurgy, University of Technology- Iraq, Baghdad, Iraq
e-mail: rasheed.mohammed40@yahoo.com

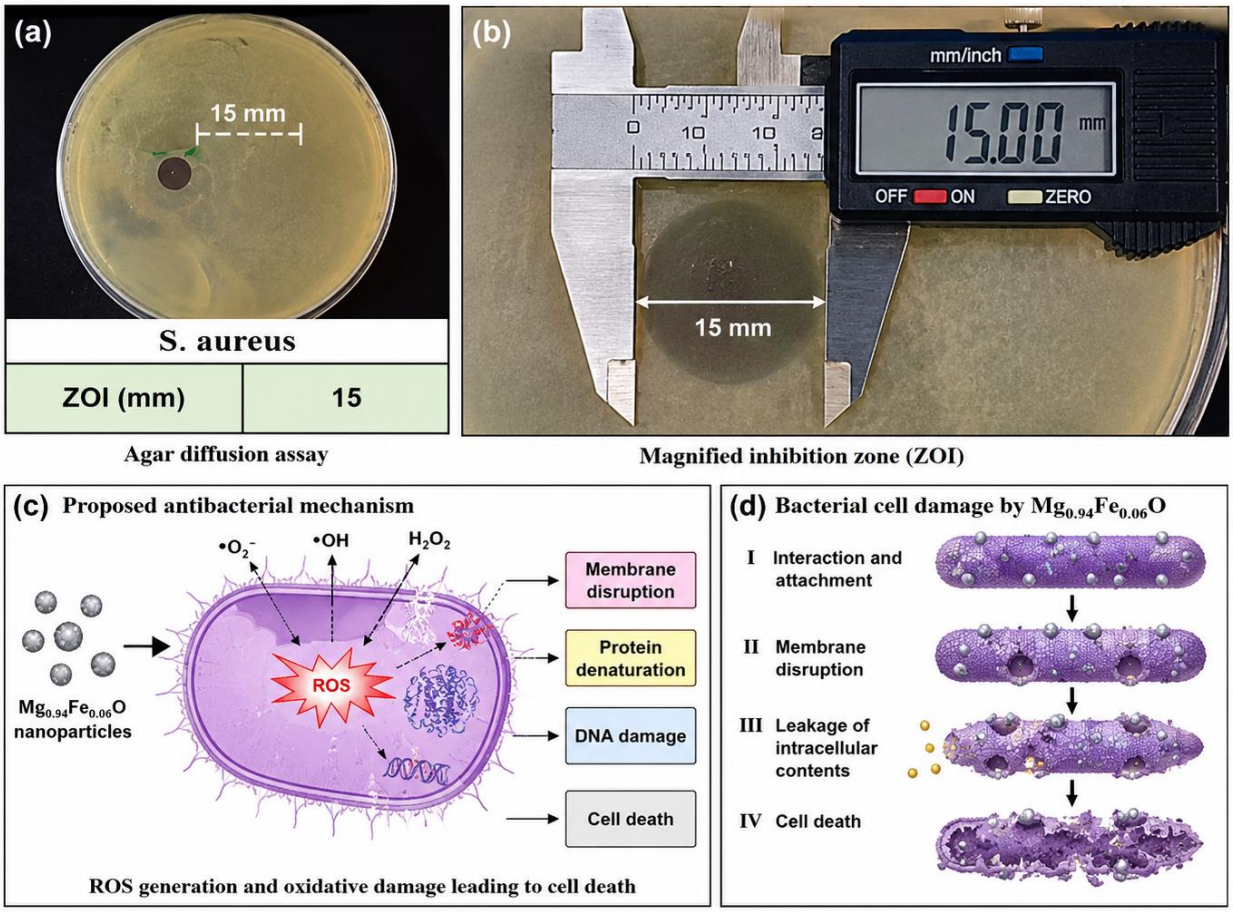

Fig. 6. (a) Agar diffusion assay showing the antibacterial activity of $Mg_{0.94}Fe_{0.06}O$ nanoparticles against *Staphylococcus aureus* with a zone of inhibition (ZOI) of approximately 15 mm; (b) magnified measurement of the inhibition zone using a digital Vernier caliper; (c) proposed antibacterial mechanism involving reactive oxygen species (ROS) generation, membrane disruption, protein denaturation, and DNA damage; and (d) schematic illustration of the sequential stages of bacterial cell destruction leading to complete bacterial cell death

STRUCTURE–PROPERTY RELATIONSHIP

The overall performance of $Mg_{0.94}Fe_{0.06}O$ nanoparticles is governed by a strong interrelationship between their structural characteristics, electronic properties, and antibacterial behavior. The characterization results obtained from FTIR, UV–Visible spectroscopy, Tauc analysis, and antibacterial evaluation collectively demonstrate that Fe incorporation modifies the crystal structure of MgO, which subsequently influences the generation of reactive oxygen species (ROS) and ultimately enhances antibacterial activity. The proposed structure–property relationship is summarized schematically in Figure 7. As illustrated in Figure 7, the incorporation of Fe^{3+} ions into the MgO crystal lattice represents the first step in enhancing the antibacterial performance of the nanoparticles. Because the ionic radius and valence state of Fe^{3+} differ from those of Mg^{2+}, partial substitution within the MgO lattice introduces local structural distortion to maintain charge neutrality. These structural changes generate a considerable number of lattice defects, including dislocations, interstitial defects, and lattice strain, which modify both the crystal structure and the electronic properties of the nanoparticles. The formation of lattice defects subsequently promotes the generation of oxygen vacancies (V_o), which are considered one of the most important active defects in metal oxide semiconductors. Oxygen vacancies act as electron-trapping centers and adsorption sites for molecular oxygen, thereby improving charge separation and reducing electron–hole recombination. Consequently, photogenerated charge carriers remain active for longer periods, increasing the efficiency of surface redox reactions.

*Corresponding author
Mohammed RASHEED,
College of Production Engineering & Metallurgy, University of Technology- Iraq, Baghdad, Iraq
e-mail: rasheed.mohammed40@yahoo.com

The increased concentration of oxygen vacancies significantly enhances the production of reactive oxygen species (ROS). Under ultraviolet irradiation or ambient oxidative conditions, photogenerated electrons react with dissolved oxygen molecules to produce superoxide radicals ($\bullet O_2^-$), while photogenerated holes oxidize surface hydroxyl groups and adsorbed water molecules to generate hydroxyl radicals ($\bullet OH$). Simultaneously, the Fe^{3+}/Fe^{2+} redox cycle facilitates continuous electron transfer and promotes Fenton-like reactions, producing additional hydrogen peroxide (H_2O_2) and hydroxyl radicals. Therefore, Fe doping not only introduces structural defects but also increases the efficiency of ROS generation by improving charge-carrier separation and accelerating interfacial redox reactions.

The generated ROS subsequently attack the bacterial cell envelope through oxidative membrane damage. Hydroxyl radicals initiate lipid peroxidation, leading to disruption of membrane phospholipids, while superoxide radicals and hydrogen peroxide oxidize membrane proteins and peptidoglycan components. As membrane permeability increases, intracellular materials—including potassium ions, proteins, enzymes, nucleic acids, and metabolites—leak into the surrounding medium. The damaged membrane also loses its ability to maintain the electrochemical gradient required for ATP synthesis and normal metabolic activity. Following membrane disruption, ROS penetrate into the bacterial cytoplasm, where they induce protein denaturation, enzyme inactivation, oxidation of amino acid residues, and fragmentation of DNA molecules. These intracellular damages inhibit DNA replication, transcription, protein biosynthesis, and energy metabolism. The simultaneous destruction of multiple cellular targets eventually causes irreversible oxidative stress and complete bacterial cell death. The antibacterial results presented in Fig. 6 clearly support this mechanism, where $Mg_{0.94}Fe_{0.06}O$ nanoparticles produced an inhibition zone of approximately 15 mm against *Staphylococcus aureus*. The excellent antibacterial activity is therefore not attributed solely to the intrinsic properties of MgO but rather to the synergistic effects introduced by Fe doping. The structural modifications generated through iron incorporation increase oxygen-vacancy concentration, improve charge-carrier dynamics, enhance ROS production, and strengthen oxidative damage to bacterial cells. The structural characterization further supports this correlation. The FTIR spectrum (Fig. 3) confirmed the successful formation of Mg–O bonds together with abundant surface hydroxyl groups and oxygen-containing functional groups, which serve as active sites for ROS formation. The UV–Visible absorption spectrum (Fig. 4) demonstrated efficient ultraviolet absorption, while the Tauc analysis (Fig. 5) revealed a wide optical band gap of 3.96 eV, confirming the semiconducting behavior required for electron–hole pair generation. These electronic characteristics, combined with the Fe-induced structural defects, explain the improved antibacterial performance observed experimentally. This structure–property correlation demonstrates that careful engineering of the crystal structure through transition-metal doping provides an effective strategy for designing highly efficient antibacterial metal oxide nanomaterials. The findings indicate that Fe-doped MgO nanoparticles possess considerable potential for advanced biomedical coatings, wound dressings, implant surface modification, food-packaging materials, water-treatment technologies, and antimicrobial healthcare products.

*Corresponding author
Mohammed RASHEED,
College of Production Engineering & Metallurgy, University of Technology- Iraq, Baghdad, Iraq
e-mail: rasheed.mohammed40@yahoo.com

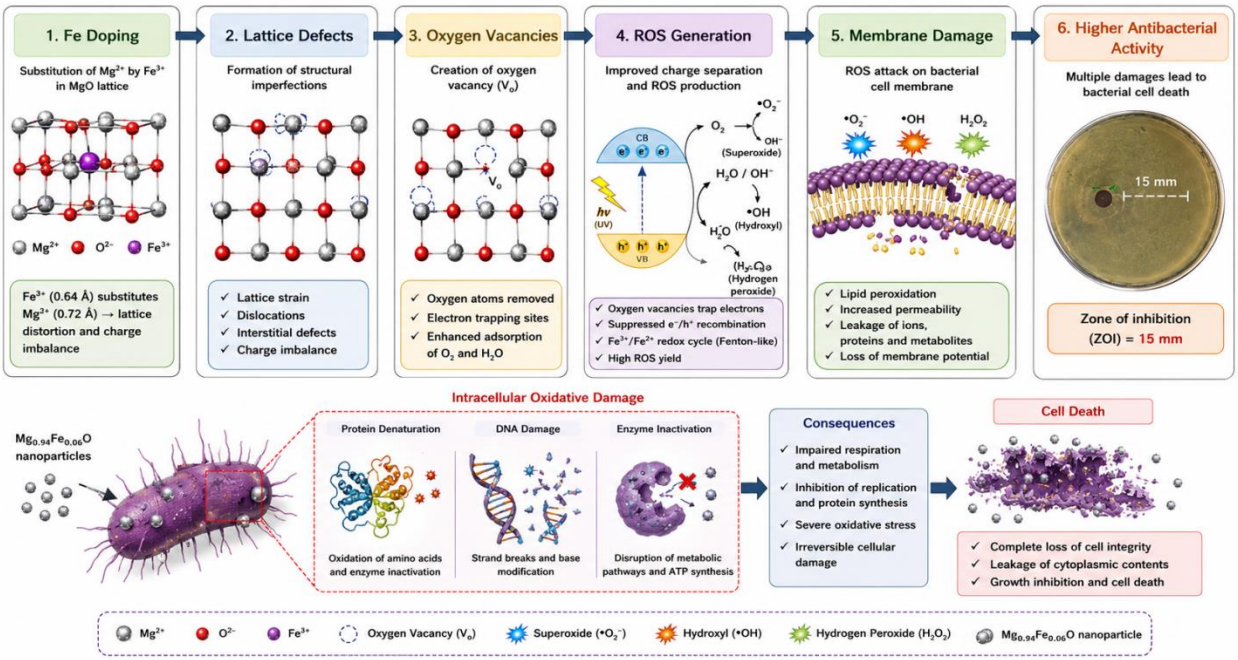

Fig. 7. Schematic illustration of the structure–property relationship of $Mg_{0.94}Fe_{0.06}O$ nanoparticles, showing how Fe doping induces lattice defects and oxygen vacancies, enhances charge-carrier separation and reactive oxygen species generation, promotes bacterial membrane disruption and intracellular oxidative damage, and ultimately improves antibacterial activity against *Staphylococcus aureus*.

CONCLUSION

Iron-doped magnesium oxide nanoparticles with the nominal composition $Mg_{0.94}Fe_{0.06}O$ were successfully synthesized through a simple chemical route followed by calcination at 550 °C. Structural and optical characterization confirmed the successful formation of Fe-doped MgO nanoparticles with properties suitable for antibacterial applications. FTIR spectroscopy revealed the characteristic Mg–O vibration together with hydroxyl functional groups that enhance surface reactivity and facilitate interactions with bacterial cell membranes. UV–Visible spectroscopy demonstrated strong ultraviolet absorption, while Tauc analysis estimated a direct optical band gap of approximately 3.96 eV, confirming the semiconducting behavior of the synthesized nanoparticles. Antibacterial evaluation against *Staphylococcus aureus* showed a clear inhibition zone of approximately 15 mm, indicating effective suppression of bacterial growth. The enhanced antibacterial performance is attributed to structural modifications induced by iron incorporation, including increased oxygen vacancy concentration, improved charge separation, greater surface defect density, and enhanced reactive oxygen species generation. These factors collectively promote oxidative stress, membrane disruption, protein denaturation, and eventual bacterial cell death. The results establish a direct relationship between structural properties and antibacterial performance, demonstrating that controlled Fe doping is an effective strategy for improving the biological activity of MgO nanoparticles. Although the present investigation was limited to a single Fe concentration and one bacterial strain, the findings provide valuable insight into the design of advanced antibacterial nanomaterials. Future research should include comprehensive structural characterization using XRD, SEM, TEM, and XPS, evaluation against a broader range of microorganisms, cytotoxicity assessment, ROS quantification, and optimization of Fe concentration to maximize antibacterial efficiency while maintaining excellent biocompatibility for practical biomedical and environmental applications.

REFERENCES

[1] M. Rasheed, I. Alshalal, A. A. Rashed, M. A. Sarhan, A. S. Jaber, Indonesian Journal of Electrical Engineering and Computer Science, **33** (2024) 653. https://doi.org/10.11591/ijeecs.v33.i1.pp653-660.

*Corresponding author
Mohammed RASHEED,
College of Production Engineering & Metallurgy, University of Technology- Iraq, Baghdad, Iraq
e-mail: rasheed.mohammed40@yahoo.com

[2] F. Boudou, A. Guendouzi, A. Belakredar, M. RASHEED, *Notulae Scientia Biologicae*, **16** (2024) 13837. https://doi.org/10.55779/nsb16211837.
[3] F. Boudou, A. Belakredar, A. Berkane, M. RASHEED, *Notulae Scientia Biologicae*, **17** (2025) 12183. https://doi.org/10.55779/nsb17212183.
[4] K. K. Khudair, F. Boudou, A. Mohammed, A. Sehmi, A. Belakredar, M. S. Ibrahim, Experimental and Theoretical NANOTECHNOLOGY, **10** (2026) 869. https://doi.org/10.56053/10.S.869.
[5] A. R. J. Katae, H. H. Hussein, A. S. Jaber, M. A. Sarhan, M. RASHEED, Experimental and Theoretical NANOTECHNOLOGY, **10** (2026) 725. https://doi.org/10.56053/10.2.725.
[6] A. R. J. Katae, H. H. Hussein, A. S. Jaber, M. A. Sarhan, M. RASHEED, Experimental and Theoretical NANOTECHNOLOGY, **10** (2026) 795. https://doi.org/10.56053/10.2.795
[7] I. M. Mohammed, M. Rasheed, *AIP Conference Proceedings*, **3321** (2025) 020026. https://doi.org/10.1063/5.0289719.
[8] M. Enneffati, M. Rasheed, B. Louati, K. Guidara, R. Barillé, Optical and Quantum Electronics, **51** (2019) 1. https://doi.org/10.1007/s11082-019-2015-5.
[9] M. S. Ibrahim, T. T. Issa, B. Yaqoob, E. N. Fayyadh, A. Rashid, R. S. Mahmood, Experimental and Theoretical NANOTECHNOLOGY, **10** (2026) 887. https://doi.org/10.56053/10.S.887.
[10] H. K. Aity, M. Rasheed, E. Dhahri, A. A. Hateef, T. Saidani, Journal of Materials Science, **61** (2026) 6226. https://doi.org/10.1007/s10853-026-12241-w.
[11] A. Khaleefah, M. RASHEED, *Experimental and Theoretical NANOTECHNOLOGY*, **10** (2026) 289. https://doi.org/10.56053/10.s.289.
[12] A. I. A. Ali, M. RASHEED, *Experimental and Theoretical NANOTECHNOLOGY*, **10** (2026) 277. https://doi.org/10.56053/10.s.277.
[13] A. I. A. Ali, M. RASHEED, *Experimental and Theoretical NANOTECHNOLOGY*, **10** (2026) 239. https://doi.org/10.56053/10.s.239.
[14] M. Rasheed, M. N. Mohammedali, F. A. Sadiq, M. A. Sarhan, T. Saidani, *Journal of Optics*, **54** (2024) 1. https://doi.org/10.1007/s12596-024-01928-5.
[15] H. M. I. Al-Zuhairi, I. Alshalal, H. H. Abbood, M. Al Nuaimi, Experimental and Theoretical NANOTECHNOLOGY, **10** (2026) 855. https://doi.org/10.56053/10.S.855.
[16] H. M. I. Al-Zuhairi, I. Alshalal, H. H. Abbood, M. Al Nuaimi, Experimental and Theoretical NANOTECHNOLOGY, **10** (2026) 1093. https://doi.org/10.56053/10.S.1093.
[17] S. S. Batros, M. Rasheed, H. K. Aity, A. A. Hatef, T. Saidani, Materials Chemistry and Physics, **355** (2026) 132243. https://doi.org/10.1016/j.matchemphys.2026.132243.
[18] Z. S. Ahmed, M. RASHEED, H. S. Ahmed, Experimental and Theoretical NANOTECHNOLOGY, **10** (2026) 329. https://doi.org/10.56053/10.s.329.
[19] Z. S. Ahmed, M. RASHEED, H. S. Ahmed, Experimental and Theoretical NANOTECHNOLOGY, **10** (2026) 343. https://doi.org/10.56053/10.s.343.
[20] A. Zubaidi, L. M. Asaad, I. Alshalal, M. Rasheed, Journal of the Mechanical Behavior of Materials, **32** (2023) 1. https://doi.org/10.1515/jmbm-2022-0302.
[21] T. Saidani, M. Rasheed, I. Alshalal, A. A. Rashed, M. A. Sarhan, R. Barillé, Research on Engineering Structures and Materials, **9** (2023) 1. https://doi.org/10.17515/resm2023.21ma0922rs.
[22] M. Rasheed, et al., Journal of Advanced Biotechnology and Experimental Therapeutics, **6** (2023) 495. https://doi.org/10.5455/jabet.2023.d144.
[23] E. Kadri, et al., Journal of Alloys and Compounds, **705** (2017) 708. https://doi.org/10.1016/j.jallcom.2017.02.117.
[24] M. Rasheed, R. Barillé, Journal of Alloys and Compounds, **728** (2017) 1186. https://doi.org/10.1016/j.jallcom.2017.09.084.
[25] R. S. Mahmood, et al., *Journal of the Mechanical Behavior of Materials*, **34** (2025) 1. https://doi.org/10.1515/jmbm-2025-0040.
[26] M. Enneffati, B. Louati, K. Guidara, M. Rasheed, R. Barillé, Journal of Materials Science: Materials in Electronics, **29** (2018) 171. https://doi.org/10.1007/s10854-017-7901-7.
[27] F. Dkhilalli, S. Megdiche, K. Guidara, M. Rasheed, R. Barillé, M. Megdiche, Ionics, **24** (2018) 169. https://doi.org/10.1007/s11581-017-2193-8.

*Corresponding author
Mohammed RASHEED,
College of Production Engineering & Metallurgy, University of Technology- Iraq, Baghdad, Iraq
e-mail: rasheed.mohammed40@yahoo.com

[28] A. Keziz, M. Rasheed, M. Heraiz, F. Sahnoune, A. Latif, *Ceramics International*, **49** (2023) 37423. https://doi.org/10.1016/j.ceramint.2023.09.068.
[29] F. Boudou, A. E. Sabar, M. I. Majeed, A. M. Ibraham, R. Jamal, A. Rashid, A. Belakredar, M. Bendahmane-Salmi, M. RASHEED, R. RASHEED, T. Saidani, H. D. Al-Bahadli, Experimental and Theoretical NANOTECHNOLOGY, **10** (2026) 821. https://doi.org/10.56053/10.S.821.
[30] D. Kherifi, A. Keziz, M. Rasheed, A. Oueslati, Ceramics International, **50** (2024) 1. https://doi.org/10.1016/j.ceramint.2024.05.317.
[31] A. J. Hussein, M. N. Al-Darraji, M. Rasheed, M. A. Sarhan, IOP Conference Series: Earth and Environmental Science, **1262** (2023) 022005. https://doi.org/10.1088/1755-1315/1262/2/022005.
[32] H. K. Aity, E. Dhahri, M. Rasheed, Ceramics International, **50** (2024) 54666. https://doi.org/10.1016/j.ceramint.2024.10.324.
[33] W. Saidi, N. Hfaidh, M. Rasheed, M. Girtan, A. Megriche, M. El Maaoui, RSC Advances, **6** (2016) 68819. https://doi.org/10.1039/c6ra15060h.
[34] A. J. Hussein, M. N. Al-Darraji, M. Rasheed, IOP Conference Series: Earth and Environmental Science, **1262** (2023) 022007. https://doi.org/10.1088/1755-1315/1262/2/022007.
[35] T. Saidani, S. Mokhtari, M. Rasheed, H. Lahmar, M. Trari, Journal of the Indian Chemical Society, **103** (2026) 102499. https://doi.org/10.1016/j.jics.2026.102499.
[36] A. Raghdi, M. Heraiz, M. Rasheed, A. Keziz, Journal of the Indian Chemical Society, **101** (2024) 101413. https://doi.org/10.1016/j.jics.2024.101413.
[37] T. Rashid, M. M. Mokji, M. Rasheed, Journal of the Mechanical Behavior of Materials, **34** (2025) 1. https://doi.org/10.1515/jmbm-2025-0074.
[38] A. A. Hateef, E. Dhahri, M. Rasheed, H. Kadhim, Z. Abbas, N. Hassan, *Physics and Chemistry of Solid State*, **25** (2024) 801. https://doi.org/10.15330/pcss.25.4.801-810.
[39] T. Rashid, M. M. Mokji, M. Rasheed, *Journal of Optics*, **53** (2024) 1. https://doi.org/10.1007/s12596-024-02080-w.
[40] E. Arif, R. Jamal, M. RASHEED, *Experimental and Theoretical NANOTECHNOLOGY*, **10** (2026) 453. https://doi.org/10.56053/10.2.453.
[41] G. E. Alkinani, A. R. J. Katae, M. RASHEED, Experimental and Theoretical NANOTECHNOLOGY, **10** (2026) 1027. https://doi.org/10.56053/10.S.1027.
[42] T. Saidani, M. Zaabat, M. S. Aida, R. Barillé, M. Rasheed, Y. Almohamed, Journal of Materials Science: Materials in Electronics, **28** (2017) 9252. https://doi.org/10.1007/s10854-017-6660-9.
[43] M. Rasheed, A. Khaleefah, Materials Chemistry and Physics, **355** (2026) 132112. https://doi.org/10.1016/j.matchemphys.2026.132112.
[44] F. Boudou, et al., Notulae Scientia Biologicae, **17** (2025) 12593. https://doi.org/10.55779/nsb17312593.
[45] M. Rasheed, S. Shihab, O. Alabdali, A. Rashid, T. Rashid, Journal of Physics: Conference Series, **1999** (2021) 012077. https://doi.org/10.1088/1742-6596/1999/1/012077.
[46] A. Aukštuolis, et al., Proceedings of the Romanian Academy Series A: Mathematics, Physics, Technical Sciences, Information Science, **18** (2017) 34. https://hal.archives-ouvertes.fr/hal-02443179.
[47] E. Kadri, M. Krichen, R. Mohammed, A. Zouari, K. Khirouni, Optical and Quantum Electronics, **48** (2016) 1. https://doi.org/10.1007/s11082-016-0812-7.
[48] M. Rasheed, O. Y. Mohammed, S. Shihab, A. Al-Adili, Journal of Physics: Conference Series, **1795** (2021) 012042. https://doi.org/10.1088/1742-6596/1795/1/012042.
[49] A. A. Abdulrahman, M. Rasheed, S. Shihab, Journal of Physics: Conference Series, **1879** (2021) 022118. https://doi.org/10.1088/1742-6596/1879/2/022118.
[50] A. Jaber, M. Ismael, T. Rashid, M. A. Sarhan, M. Rasheed, I. M. Sala, Eureka: Physics and Engineering, **4** (2023) 29. https://doi.org/10.21303/2461-4262.2023.002770.

*Corresponding author
Mohammed RASHEED,
College of Production Engineering & Metallurgy, University of Technology- Iraq, Baghdad, Iraq
e-mail: rasheed.mohammed40@yahoo.com